Nuclear Instruments and Methods in Physics Research B xxx (2014) xxx–xxx

Contents lists available at ScienceDirect

Nuclear Instruments and Methods in Physics Research B

journal homepage: www.elsevier.com/locate/nimb

Influence of radiation damage on xenon diffusion in silicon carbide

E. Friedland [a,*], K. Gärtner [b], T.T. Hlatshwayo [a], N.G. van der Berg [a], T.T. Thabethe [a]

[a] Physics Department, University of Pretoria, Pretoria, South Africa
[b] Institut für Festkörperphysik, Friedrich-Schiller-Universität, Jena, Germany

ARTICLE INFO

Article history:
Available online xxxx

Keywords:
Silicon carbide
Diffusion
Radiation damage

ABSTRACT

Diffusion of xenon in poly and single crystalline silicon carbide and the possible influence of radiation damage on it are investigated. For this purpose 360 keV xenon ions were implanted in commercial 6H-SiC and CVD-SiC wafers at room temperature, 350 °C and 600 °C. Width broadening of the implantation profiles and xenon retention during isochronal and isothermal annealing up to temperatures of 1500 °C was determined by RBS-analysis, whilst in the case of 6H-SiC damage profiles were simultaneously obtained by α-particle channelling. No diffusion or xenon loss was detected in the initially amorphized and eventually recrystallized surface layer of cold implanted 6H-SiC during annealing up to 1200 °C. Above that temperature serious erosion of the implanted surface occurred, which made any analysis impossible. No diffusion or xenon loss is detected in the hot implanted 6H-SiC samples during annealing up to 1400 °C. Radiation damage dependent grain boundary diffusion is observed at 1300 °C in CVD-SiC.

1. Introduction

Modern high-temperature nuclear reactors (HTR's) commonly use fuel elements containing triple isotropic cladded (TRISO) fuel particles. These are fuel kernels surrounded by four successive layers of low-density pyrolitic carbon, high-density pyrolitic carbon, silicon carbide and high-density pyrolitic carbon, with silicon carbide being the main barrier to prevent the release of fission products. They retain quite effectively most of the important fission products up to temperatures of 1000 °C, which is the typical operating temperature of HTR's currently in use [1]. Design studies for the *International Generation IV Reactor Program* consider HTR's operating at temperatures significantly above 1000 °C to enhance their efficiency, especially in view of process heat applications for hydrogen generation [2]. However, little reliable information on transport properties of fission products in silicon carbide above this temperature is available.

Recently our group started a systematic study on the diffusion of environmentally relevant fission products in silicon carbide at temperatures above 1000 °C. The results for strontium, silver, iodine and cesium, with special emphasis on the influence of radiation damage on them, have been published [3–8]. The current publication reports on the transport of xenon in 6H-SiC and CVD-SiC at temperatures up to 1500 °C. Radio-active xenon isotopes are an important group of gaseous fission products and their retention in the fuel particles is therefore of crucial importance for reactor safety.

2. Experiment and analysis

Hexagonal 6H-SiC from *Intrinsic Semiconductors*® and CVD-SiC from *Valley Design Corporation*®, having a columnar structure of mainly 3C-SiC crystallites, were used in the investigations. A fluence of 1×10^{16} cm^{-2} xenon ions were implanted at room temperature (RT), 350 °C and 600 °C into the wafers with energy of 360 keV and a flux not exceeding 10^{13} cm^{-2} s^{-1} to obtain a maximum concentration of about 1%. The different implantation temperatures made it possible to compare transport processes in amorphous, poly and single crystalline silicon carbide. Diffusion was determined from the broadening of the implantation profiles after isochronal and isothermal annealing studies using RBS analysis. In the case of single crystalline samples these measurements were combined with the results of α-particle channeling spectroscopy to obtain defect density profiles as a function of implantation and annealing temperatures. Structural information on the samples before and after annealing was obtained by scanning electron microscopy (SEM) and topological surface profiles by atomic force microscopy (AFM) employing a *Bruker's Dimension Icon* scanning probe. A detailed description of the experimental techniques is given elsewhere [5].

* Corresponding author. Address: Physics Department, University of Pretoria, Private Bag Hatfield, Pretoria, South Africa. Tel.: +27 12 4202453; fax: +27 12 3625288.
E-mail address: erich.friedland@up.ac.za (E. Friedland).

http://dx.doi.org/10.1016/j.nimb.2014.02.109
0168-583X/

Diffusion coefficients were extracted from the broadening of implantation profiles during isothermal annealing. Assuming a Gaussian depth distribution the following relationship between the final and original widths holds [9],

$$[W(t)]^2 = 4Dt\ ln(2) + [W(0)]^2,$$

where $W(t)$ is defined as the full width at half-maximum after annealing for time t. Hence, the diffusion coefficient D at temperature T_a is directly obtained from the slope of a plot of $[W(t)]^2$ versus annealing time t.

For the determination of defect density profiles, Rutherford backscattering spectra were measured at room temperature for aligned (in (0001) direction) and random incidence using 1.44 MeV and 1.65 MeV α-particles. As an example, the backscattering yields for the as-implanted 6H-SiC samples are shown in Fig. 1. The resulting RBS minimum yields χ_{min} (ratio of aligned and random yield) were first analyzed with the help of the computer code DICADA [10] which makes use of a modified master equation approach based on the channelling concept of Lindhard. This code provides the relative number of displaced atoms $n_{da}(z)$ as functions of the depth z calculated from the measured minimum yield $\chi_{min}(z)$, provided that there is no correlation between the displacements. This is true for point defects, point defect clusters and amorphous zones. The displaced atoms are assumed to be randomly distributed within a lattice cell (no preferred lattice sites) which is true in the case of highly damaged crystalline targets as considered here. The analysis of the RBS data showed that in all cases the resulting point defect densities $n_{da}(z)$ remain quite high at depths large compared with the position of their maxima which is unrealistic. It is demonstrated in Fig. 2 for the as-implanted sample at 600 °C, where this effect is most pronounced. Consequently, the damage in the 6H-SiC samples cannot only consist of point defects but in addition, extended defects with correlated displaced atoms (dislocation, stacking faults) must be present. Persson et al. [11] investigated the damage in Al implanted 4H-SiC. They found point defects and dislocation loops. This may be a hint, that the ion implanted 6H-SiC also contains dislocation loops in addition to the point defects. Therefore, the defect analysis should be performed taking into account dislocation loops. But this is not possible using DICADA which is only applicable to point defects.

There exists a version of DICADA (DICADA1) which includes extended defects, however, it is applicable only to elementary targets

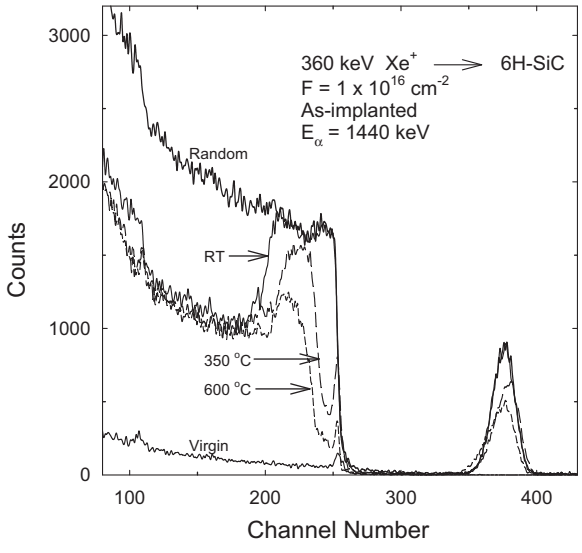

Fig. 1. Random and aligned spectra of 6H-SiC implanted at RT, 350 °C and 600 °C with a fluence of 10^{16} Xe^+ cm^{-2} at 360 keV.

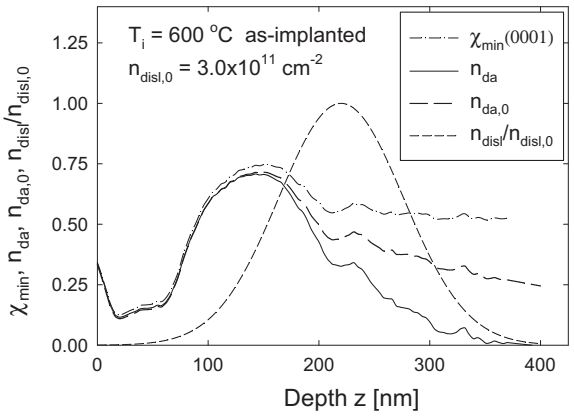

Fig. 2. Minimum yield and defect densities as functions of the depth z for 6H-SiC implanted with a fluence of 10^{16} Xe cm^{-2} at 600 °C. The point defect densities $n_{da,0}$ and n_{da} have been obtained using DICADA (only point defects) and DICADA1 (point defects and dislocation loops).

(the inclusion of dislocation loops is described in Ref. [12]). In order to be able to use DICADA1, it has been tested, whether (with respect to the defect analysis) the 6H-SiC crystal can be approximated by an 'elementary crystal 6H-SiC' with the lattice structure of the 6H-SiC lattice where all lattice sites are occupied by the same atoms with an average atomic number $Z_{2,av} = 10$ and an average atomic mass $m_{2,av} = 20.0$ amu. The other properties remain unchanged. Under the assumption, that only point defects are present, their distribution $n_{da}(z)$ has been calculated using DICADA (6H-SiC crystal) and DICADA1 ('elementary 6H-SiC crystal'). In all cases considered here, the two distributions differ less than the statistical fluctuations of the measured minimum yields. This justifies, the use of DICADA1, which provides the advantage to include dislocation loops.

All the following results of the defect densities have been obtained using DICADA1 and the 'elementary crystal 6H-SiC' with atoms of $Z_{2,av} = 10$ and $m_{2,av} = 20.0$ amu. For our calculations we used a Debye temperature of $\theta_D = 1030$ K, which is an average of the widely varying published values [13], and the lattice parameters $a = 0.3081$ nm and $c = 1.5092$ nm. The properties of the dislocation loops are less known. For the Poisson's ratio the value 0.14 given in Ref. [14] has been used. The loops are assumed to lay in the (0001) plane with the Burger's vector in ⟨0001⟩ direction. The magnitude of the Burger's vector and the loop radius are chosen to be $c = 1.5092$ nm and 100 nm, respectively. Furthermore it is assumed that the density profile of the dislocation loops can be described by the Gaussian function $n_{disl}(z) = n_{disl.0}\ \exp\{-[(z - z_{max})/\sigma]^2\}$. Then, for a given set of values of $n_{disl.0}$, z_{max} and σ, the point defect density $n_{da}(z)$ has been calculated. The results show, that $n_{da}(z)$ is not very sensitive to z_{max} and σ, and for simplicity, the same values $z_{max} = 220$ nm and $\sigma = 80$ nm are used in all cases. Finally, the only free parameter $n_{disl.0}$ is chosen to minimize $n_{da}(z)$ at large depths.

Fortunately, the point defect density $n_{da}(z)$ is not much influenced by the parameters of the dislocation loops (kind of loops and their radius, orientation and magnitude of the Burgers vector), only $n_{disl.0}$ is sensitive to these parameters. Hence, the defect analysis as described above provides reliable point defect densities, which are only of interest in this paper. As an example the results for the as-implanted 6H-SiC at 600 °C, which has the highest density of dislocations, are shown in Fig. 2. The point defect density $n_{da}(z)$ obtained by taking dislocation loops into account tends to zero at large depths, while the neglect of them leads to unrealistic high values in this region.

Please cite this article in press as: E. Friedland et al., Influence of radiation damage on xenon diffusion in silicon carbide, Nucl. Instr. Meth. B (2014), http://dx.doi.org/10.1016/j.nimb.2014.02.109

3. Results and discussion

The damage profiles of the as-implanted wafers are plotted in Fig. 3. The cold implantation leads to an amorphous surface layer in which the xenon is fully embedded. During hot implantations the crystal structure is retained, albeit it with a relatively large damage peak at 350 °C and a significantly smaller one at 600 °C. This is due to a strong temperature dependence of irradiation induced annealing, which also leads to broadening of the implantation profiles and significant xenon losses during hot implantations. The surface region of the RT-implant is up to a depth of about 200 nm completely disordered, while the density of extended defects is low. At an implantation temperature of 350 °C the basic crystal structure is retained although the density of displaced atoms is quite high. Furthermore the dislocation density is higher than in the cold implantation. The 600 °C implant displays a significantly reduced density of displaced atoms but a further increase of extended defects.

3.1. Annealing of 6H-SiC

The annealing behavior of the cold and hot implanted hexagonal samples differs fundamentally due to the completely different structure of the irradiation damage. SEM observations show that the amorphous region of the cold implant recrystallizes into a finely grained polycrystalline structure after a short annealing period at relatively low temperature, which cannot be removed even after prolonged annealing. After annealing for 5 h at 1300 °C large crystals have grown, modifying the surface topology significantly.

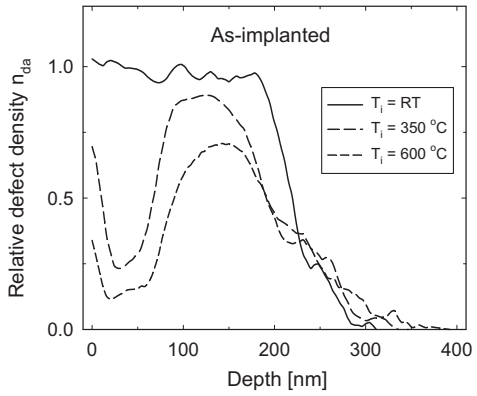

Fig. 3. Defect profiles in 6H-SiC after implantation at RT, 350 °C and 600 °C with a fluence of 10^{16} Xe^+ cm^{-2} at 360 keV.

In contrast to this the radiation damage of the hot implants is gradually reduced during annealing, while their single crystalline structure is maintained. However, thermal etching becomes important at higher temperatures and will eventually erode the surface area. At 1300 °C this effect is still very modest for the hot implants; AFM profiling yields an average surface roughness of approximately 10 nm after 40 h annealing.

Isochronal annealing curves of 6H-SiC-implants for different implantation temperatures, depicting the profile widths and the retention of xenon, are shown in Fig. 4. For cold implantation, the α-particle channelling spectra and defect profiles are depicted in Fig. 5. During the initial annealing steps up to 1200 °C the original amorphous layer transforms into a somewhat thinner polycrystalline layer due to epitaxial regrowth from the undamaged bulk. No diffusion and no xenon loss are observed during this period. A slight width broadening together with a significant change of the defect profile's shape is taking place during the next annealing step at 1300 °C. However, a close inspection of the appropriate aligned spectrum reveals, that this is not due to diffusion but that it indicates the beginning of surface erosion of the sample. This erosion becomes serious at 1400 °C, where it leads to significant xenon loss.

The evolution of defect profiles of implants at 350 °C and 600 °C during isochronal annealing is depicted in Fig. 6. For both implantation temperatures a similar trend is observed. The damage densities are significantly reduced during each annealing step. Although the 350 °C implant starts from a higher level, both reach the same defect density after the last annealing step at 1400 °C. A further annealing step at 1500 °C resulted in surface erosion and was therefore not analysed. The broadening of the xenon peak and the loss of xenon during that last step shown in Fig. 4 is probably due to surface roughening. Hence, despite the strong reduction of damage during isochronal annealing, no diffusion or loss of xenon is observed up to a temperature of 1400 °C.

Isothermal annealing curves at T_a = 1200 °C and T_a = 1300 °C together with the accompanying damage profiles for the implantation temperature of 600 °C are depicted in Fig. 7. During the first 5 h of annealing the damage density is strongly reduced, while very little change occurs during the following annealing cycles. Similarly as during isochronal annealing, no width broadening of the xenon peaks and no xenon loss is observed within experimental uncertainty.

3.2. Annealing of CVD-SiC

Isothermal annealing curves at T_a = 1200 °C and T_a = 1300 °C for CVD-SiC implanted at RT and 350 °C are given in Fig. 8. Fast xenon transport is observed in the cold implanted samples, especially in

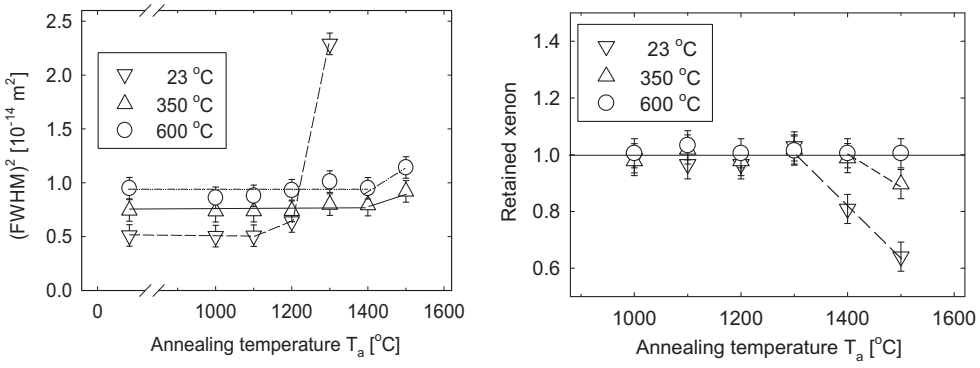

Fig. 4. Isochronal annealing curves (t_a = 5 h) for 6H-SiC implanted at RT, 350 °C and 600 °C. The two graphs show the profile widths and the part of retained xenon as a function of annealing temperature T_a.

Please cite this article in press as: E. Friedland et al., Influence of radiation damage on xenon diffusion in silicon carbide, Nucl. Instr. Meth. B (2014), http://dx.doi.org/10.1016/j.nimb.2014.02.109

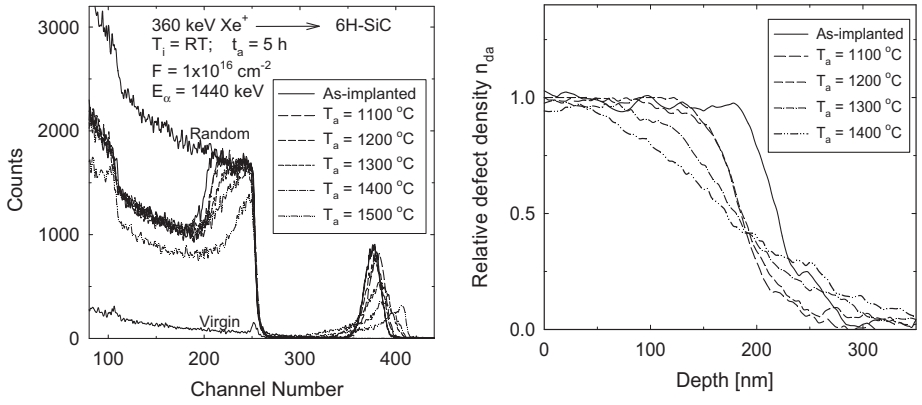

Fig. 5. Random and aligned spectra of 6H-SiC implanted at RT before and after isochronal annealing (t_a = 5 h) and the corresponding damage profiles.

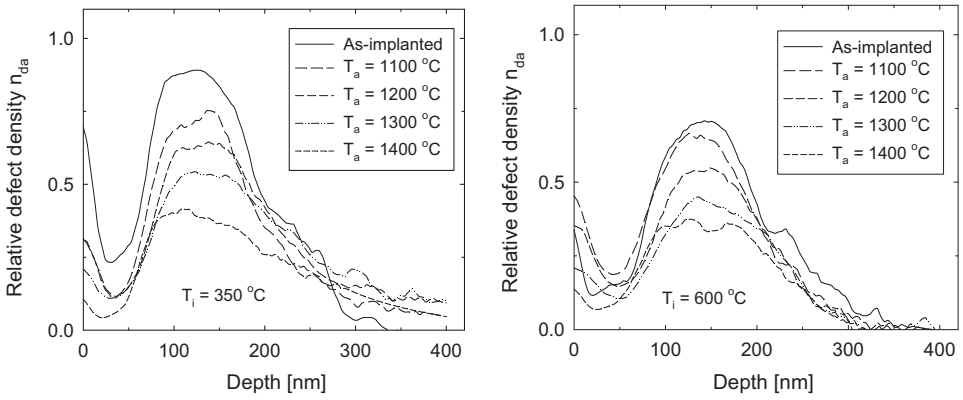

Fig. 6. Defect profiles during isochronal annealing (t_a = 5 h) of 6H-SiC implanted at 350 °C and 600 °C.

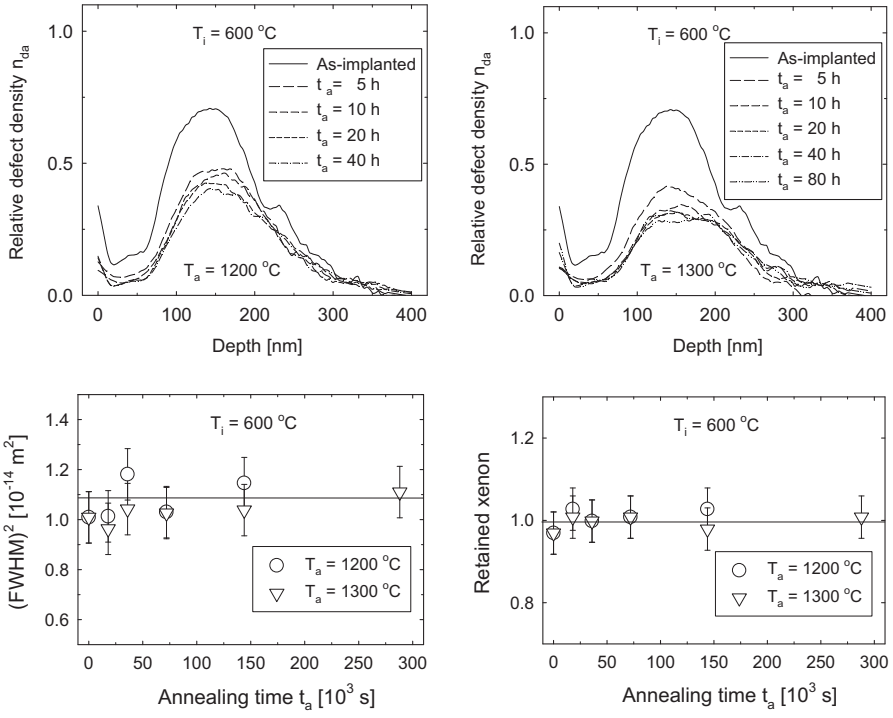

Fig. 7. Isothermal defect profiles, as well as annealing and part of retained xenon curves for 6H-SiC at T_a = 1200 °C and T_a = 1300 °C, implanted at 600 °C.

Please cite this article in press as: E. Friedland et al., Influence of radiation damage on xenon diffusion in silicon carbide, Nucl. Instr. Meth. B (2014), http://dx.doi.org/10.1016/j.nimb.2014.02.109

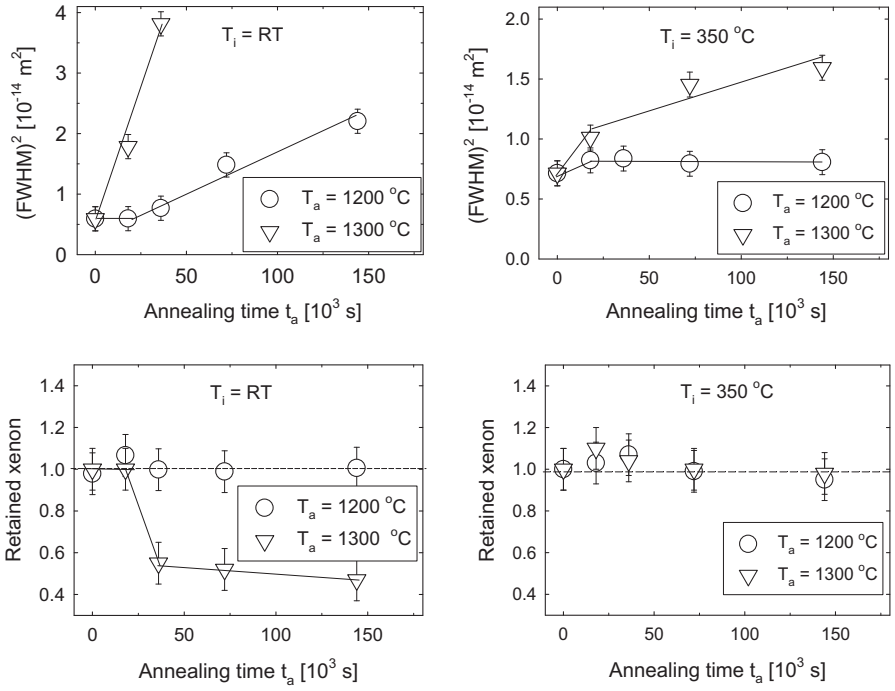

Fig. 8. Isothermal annealing and part of retained xenon curves for CVD-SiC at T_a = 1200 °C and T_a = 1300 °C, implanted at RT and 350 °C.

that one annealed at the higher temperature. The hot implanted samples show relatively strong diffusion during the first annealing cycle, which reduces to a modest rate at the higher annealing temperature and stops altogether at the lower one. No xenon loss occurs during annealing in the hot implant. However, the cold implant loses about 50% of the implanted xenon during the second annealing cycle of 5 h at 1300 °C, while very little further loss occurs during the remaining 30 h. As no diffusion up to 1400 °C was observed for the 6H-SiC, the diffusion of xenon in CVD-SiC must be due to grain boundary diffusion.

4. Conclusions

Irradiation induced diffusion leads to significant xenon loss in 6H-SiC during implantation at high temperatures. At 350 °C and 600 °C the losses are 23% and 31% respectively compared with implantation at RT. Contrary to this no diffusion is observable during isochronal or isothermal annealing up to 1200 °C in cold and up to 1400 °C in hot implants. At higher temperatures the onset of surface erosion made measurements unreliable. Even during the initial annealing stage, when the xenon is still embedded in either amorphous or highly damaged crystalline matter, no diffusion is detectable. This is quite remarkable, as such initial diffusion was generally observed with other diffusors [8]. The reason might be that xenon does not easily form defect complexes, but rather segregates into immobile planar clusters with an epitaxial alignment in the hexagonal crystal structure of the substrate.

In CVD-SiC diffusion occurs along grain boundaries at temperatures above 1200 °C. Grain boundaries are known to be sinks for defects and their structure should therefore depend strongly on the irradiation damage incurred during implantation. The sample amorphized during RT-implantation shows no diffusion during the first annealing cycle at 1200 °C, but strong diffusion starts from then on. A diffusion coefficient of approximately 10^{-19} m^2 s^{-1} is extracted from the slope of the annealing curve. At 1300 °C extreme profile broadening is observed, which probably is mainly due to surface erosion. During the second annealing cycle about half of the xenon is lost, which most likely constitutes the fraction assembled in the newly formed grain boundaries. Very little further loss occurs during prolonged annealing, indicating that the remaining xenon is situated within the crystallites. The isothermal annealing curves for the hot implant displays the typical behavior found with other diffusors [8]. Relatively large xenon transport takes place during the first annealing cycle, with a significantly reduced rate at longer annealing times. At 1200 °C it is below the experimental detection limit of 10^{-21} m^2 s^{-1}, while at 1300 °C a diffusion coefficient of 5×10^{-20} m^2 s^{-1} is obtained.

On the reason for the different diffusion properties of volume and grain boundary diffusion after hot implantation can only be speculated. A possible explanation is that the above suggested xenon segregation into hexagonal planar configurations might not be favored in grain boundaries, where the structure is highly distorted and warped.

Acknowledgements

Financial support of the *National Research Foundation* and the *Bundesministerium für Bildung und Forschung* is gratefully acknowledged. Thanks are due to Elke Wendler, who arranged the implantations by the ion beam group of the *Institut für Festkörperphysik* in Jena.

References

[1] D. Hanson, A Review of Radionuclide Release from HTGR Cores During Normal Operation, Electric Power Research Institute, Report 1009382, March 2004.
[2] National Hydrogen Energy Roadmap, United States Department of Energy, Washington, DC, November 2002.
[3] E. Friedland, J.B. Malherbe, N.G. van der Berg, T. Hlatshwayo, A.J. Botha, E. Wendler, W. Wesch, J. Nucl. Mater. 389 (2009) 326.
[4] E. Friedland, N.G. van der Berg, J.B. Malherbe, R.J. Kuhudzai, A.J. Botha, E. Wendler, W. Wesch, Nucl. Instr. Meth. B 268 (2010) 2892.
[5] E. Friedland, N.G. van der Berg, J.B. Malherbe, J.J. Hanke, J. Barry, E. Wendler, W. Wesch, J. Nucl. Mater. 410 (2011) 24.
[6] E. Friedland, N.G. van der Berg, J.B. Malherbe, E. Wendler, W. Wesch, J. Nucl. Mater. 425 (2012) 205.
[7] E. Friedland, N.G. van der Berg, T.T. Hlatshwayo, R.J. Kuhudzai, J.B. Malherbe, E. Wendler, W. Wesch, Nucl. Instr. Meth. B 286 (2012) 102.

Please cite this article in press as: E. Friedland et al., Influence of radiation damage on xenon diffusion in silicon carbide, Nucl. Instr. Meth. B (2014), http://dx.doi.org/10.1016/j.nimb.2014.02.109

[8] E. Friedland, T.T. Hlatshwayo, N.G. van der Berg, Phys. Status Solidi C 10 (2013) 208.
[9] S.M. Myers, S.T. Picraux, T.S. Prevender, Phys. Rev. B 9 (1974) 3953.
[10] K. Gärtner, Nucl. Instr. Meth. B 227 (2005) 522.
[11] P.O.Å. Persson, L. Hultman, M.S. Janson, A. Hallén, J. Appl. Phys. 100 (2006) 53521.
[12] K. Gärtner, A. Ugguzoni, Nucl. Instr. Meth. B 67 (1992) 189.
[13] L.L. Snead, T. Nozawa, Y. Katoh, T.-S. Byun, S. Kondo, D.A. Petty, J. Nucl. Mater. 371 (2007) 329.
[14] Silicon Carbide Properties, www.accuratus.com.

Please cite this article in press as: E. Friedland et al., Influence of radiation damage on xenon diffusion in silicon carbide, Nucl. Instr. Meth. B (2014), http://dx.doi.org/10.1016/j.nimb.2014.02.109